

SPECTROSCOPIC ANALYSIS OF METAL-POOR STARS FROM LAMOST: EARLY RESULTS

HAI-NING LI¹, GANG ZHAO¹, NORBERT CHRISTLIEB², LIANG WANG¹, WEI WANG¹, YONG ZHANG³, YONGHUI HOU³, AND HAILONG YUAN¹

(Received ; Accepted)
Draft version June 28, 2021

ABSTRACT

We report on early results from a pilot program searching for metal-poor stars with LAMOST and follow-up high-resolution observation acquired with the MIKE spectrograph attached to the Magellan II telescope. We performed detailed abundance analysis for eight objects with iron abundances $[\text{Fe}/\text{H}] < -2.0$, including five extremely metal-poor (EMP; $[\text{Fe}/\text{H}] < -3.0$) stars with two having $[\text{Fe}/\text{H}] < -3.5$. Among these objects, three are newly discovered EMP stars, one of which is confirmed for the first time with high-resolution spectral observations. Three program stars are regarded as carbon-enhanced metal-poor (CEMP) stars, including two stars with no enhancement in their neutron-capture elements, which thus possibly belong to the class of CEMP-no stars; one of these objects also exhibits significant enhancement in nitrogen, and is thus a potential carbon and nitrogen-enhanced metal-poor star. The $[\text{X}/\text{Fe}]$ ratios of the sample stars generally agree with those reported in the literature for other metal-poor stars in the same $[\text{Fe}/\text{H}]$ range. We also compared the abundance patterns of individual program stars with the average abundance pattern of metal-poor stars, and find only one chemically peculiar object with abundances of at least two elements (other than C and N) showing deviations larger than 0.5 dex. The distribution of $[\text{Sr}/\text{Ba}]$ versus $[\text{Ba}/\text{H}]$ agrees that an additional nucleosynthesis mechanism is needed aside from a single r -process. Two program stars with extremely low abundances of Sr and Ba support the prospect that both main and weak r -process may have operated during the early phase of Galactic chemical evolution. The distribution of $[\text{C}/\text{N}]$ shows that there are two groups of carbon-normal giants with different degrees of mixing. However, it is difficult to explain the observed behavior of the $[\text{C}/\text{N}]$ of the nitrogen-enhanced unevolved stars based on current data.

Subject headings: Galaxy: halo — stars: abundances — stars: Population II

1. INTRODUCTION

Very metal-poor ($[\text{Fe}/\text{H}]^4 < -2.0$) and extremely metal-poor (EMP; $[\text{Fe}/\text{H}] < -3.0$) stars are believed to preserve in their atmospheres detailed information concerning the chemical compositions of the interstellar medium at the time and place that they were born. These objects are expected to offer us a direct view into the earliest phases of the evolution of the Galaxy, the formation of the first generation of stars, and the earliest nucleosynthesis events (McWilliam et al. 1995; Norris et al. 1996; Beers & Christlieb 2005; Frebel & Norris 2013). Precise analysis of the chemical composition of metal-poor stars enables us to indirectly probe the range of supernova nucleosynthesis yields in the early Galaxy (Heger & Woosley 2010; Nomoto et al. 2013, and reference therein), and to ultimately constrain the primordial nucleosynthesis of cosmological models as well (for details, see Bromm & Yoshida 2011).

Ever since the discovery of metal-poor stars by Chamberlain & Aller (1951), numerous efforts have been devoted to related fields and remarkable progress has been achieved. To explore the nature of the first generation of stars, detailed abundance analyses based on high-resolution

spectroscopy have been performed to identify various abundance patterns in metal-deficient stars (e.g., Ryan et al. 1996; Lai et al. 2008; Cohen et al. 2008; Norris et al. 2013b). These explorations also resulted in the discovery of a variety of unusual peculiarities in elemental abundances in metal-poor stars, such as large enhancements in carbon and nitrogen relative to iron and the abundance ratios seen in the Sun; enhancement of α elements; and neutron-capture elements (Aoki et al. 2007; Pols et al. 2012; Aoki et al. 2013; Placco et al. 2013). The ever-increasing sample size of metal-poor halo stars and the enrichment history of the Galactic halo have gradually been revealed through statistical investigations in the low-metallicity region of the metallicity distribution function (MDF; Carollo et al. 2007; Schörck et al. 2009; Li et al. 2010; Yong et al. 2013b).

Recent studies using an increasing number of metal-poor stars have made it clear that there exists a large fraction in such stars with significant enhancements of carbon, i.e., carbon-enhanced metal-poor (CEMP) stars. The frequency of CEMP stars is suggested to increase with decreasing metallicity (Cohen et al. 2005; Lucatello et al. 2006; Carollo et al. 2012; Spite et al. 2013; Yong et al. 2013b). Larger samples of CEMP stars also indicate different types of chemical patterns, mainly including four sub-classes defined based on the abundances of the neutron-capture elements (Beers & Christlieb 2005): CEMP- s (enhanced in s -process elements), CEMP- r (enhanced in r -process elements), CEMP- rs (enhanced in both s - and r -process elements), and CEMP-no (no enhancement in neutron-capture elements). This diversity in chemistry suggests different sites of carbon production in the early Galaxy, and detailed analyses of the elemental abundances of CEMP stars allow us to understand the nature of their progenitor stars.

lhn@nao.cas.cn, gzhao@nao.cas.cn

¹ Key Lab of Optical Astronomy, National Astronomical Observatories, Chinese Academy of Sciences, A20 Datun Road, Chaoyang, Beijing 100012, China

² Zentrum für Astronomie der Universität Heidelberg, Landessternwarte, Königstuhl 12, D-69117 Heidelberg, Germany

³ Nanjing Institute of Astronomical Optics & Technology, National Astronomical Observatories, Chinese Academy of Sciences, Nanjing 210042, China

⁴ The notation of $[A/B] = \log(N_A/N_B)_\star - \log(N_A/N_B)_\odot$ is used here, where N_A and N_B are the number densities of elements A and B respectively, and \star and \odot refer to the star and the Sun respectively

As a key to all these investigations, the number of metal-poor stars has been tremendously increased by recent wide-angle sky surveys, including the HK survey (Beers et al. 1992) and the Hamburg/ESO survey (HES; Christlieb et al. 2008), and more recently using data from the Sloan Digital Sky Survey (York et al. 2000) and the Sloan Extension for Galactic Understanding and Exploration (SEGUE; Yanny et al. 2009; Rockosi et al. 2009), as well as the SkyMapper Telescope (Keller et al. 2007) using the novel photometric filter system.

Subsequently, high-resolution spectroscopic research has been performed for the metal-poor stars found in these surveys (e.g., McWilliam et al. 1995; Norris et al. 2001; Cohen et al. 2004; Barklem et al. 2005). Studies of large samples have been conducted, including the “First Stars” project (Cayrel et al. 2004; Bonifacio et al. 2009), the “OZ project” (Cohen et al. 2011), “The Most Metal-Poor Stars” project (Norris et al. 2013a; Yong et al. 2013a), and the “Extremely Metal-Poor Stars from SDSS/SEGUE” (Aoki et al. 2013) project. These efforts have resulted in detailed investigations of the abundances of more than 200 EMP stars, including two hyper metal-poor (HMP) stars HE 1327–2326 ($[\text{Fe}/\text{H}] = -5.4$, Frebel et al. 2005) and HE 0107–5240 ($[\text{Fe}/\text{H}] = -5.3$, Christlieb et al. 2002), and J0313–6708, a star at $[\text{Fe}/\text{H}] < -7.1$ which is suspected to have been pre-enriched by a single supernova (Keller et al. 2014).

These surveys and follow-ups have not only identified chemically peculiar low-metallicity objects and made it possible to explore the evolution of the Galactic halo in a much more detailed and systematic manner, but have also led to a number of debates. Recent discoveries of more EMP stars with $[\text{Fe}/\text{H}] < -3.5$ (Yong et al. 2013a; Placco et al. 2014) have enabled us to determine more accurately the low-metallicity tail of the MDF of the Galactic halo. It was found that the sharp cutoff at $[\text{Fe}/\text{H}] \sim -3.6$ previously observed in HES data (Schörck et al. 2009; Li et al. 2010) is probably an artifact caused by small number statistics, and that the MDF in fact smoothly decreases at least down to approximately $[\text{Fe}/\text{H}] \sim -4.1$ (Yong et al. 2013b). With extended samples of EMP stars, Placco et al. (2014) also raises doubts about the cutoff of the abundance ratio of $[\text{Sr}/\text{Ba}]$ at about $[\text{Fe}/\text{H}] \sim -3.6$, which was previously pointed out by Aoki et al. (2013). All of these unsolved questions urgently require additional EMP stars, especially objects with $[\text{Fe}/\text{H}] < -3.5$, to better understand the truth and the real picture of the earliest phases of Galactic chemical evolution.

The Large sky Area Multi-Object fiber Spectroscopic Telescope (LAMOST, also known as the Wang-Su Reflecting Schmidt Telescope or the Guoshoujing Telescope)⁵ is a new type of wide-field telescope with a large aperture (Cui et al. 2012). LAMOST started its pilot survey in 2010 (Luo et al. 2012), and has conducted a five year regular survey since 2011. The combination of a large aperture (4 m) and high multiplex factor (4000 fibers) with a 5° field of view makes it a unique facility. Its special design and high spectrum acquiring rate allow LAMOST to efficiently carry out systematic spectroscopic surveys of the various stellar components of the Galaxy (Zhao et al. 2006, 2012), including metal-poor stars. Furthermore, with the low-resolution ($R = 1800$) spectroscopic data from LAMOST, it is possible to reliably identify metal-poor stars in survey mode, thus evidently enhancing

the survey efficiency. Therefore, we are using this facility to further increase the number of metal-poor stars.

This paper is organized as follows. Observations and data reduction are addressed in Section 2. The determination of stellar parameters and abundance analysis are described in Section 3. The interpretations and discussions of the derived elemental abundances including comparisons with literature values are presented in Section 4. The conclusions are given in Section 5.

2. TARGET SELECTION AND OBSERVATION

Sample stars were selected from the low-resolution database ($R = 1800$) spectra acquired with LAMOST. After robust estimation of stellar parameters and selection of candidates using LAMOST data, high-resolution ($R \sim 35,000$) spectroscopy was obtained for eight interesting objects with Magellan/MIKE to carry out detailed abundance analysis of these stars.

2.1. Low-resolution Spectroscopic Observation with LAMOST

Our study is based on the first data release of the LAMOST survey which was internally released after the first year of LAMOST survey operations. The wavelength coverage (3700–9100 Å) and resolving power ($R = 1800$) of the LAMOST spectra allow a robust estimation of the stellar parameters, including metallicities. Three independent methods are used to determine the metallicity of an object.

The first method is an application of an updated version of the methods described by Beers et al. (1999), which obtain $[\text{Fe}/\text{H}]$ by making use of the Ca II K line index KP measuring the strength of this line and the HP2 index measuring the strength of the H_δ line. This method has also been adopted by previous investigations such as Schörck et al. (2009) to which we refer the reader for details.

The other two methods make use of a grid of synthetic spectra. These spectra were computed by using the synthesis code SPECTRUM (Gray & Corbally 1994), starting from the ATLAS9 grid of stellar atmospheric models of Castelli & Kurucz (2003) with linear interpolation in three dimensions, i.e., T_{eff} , $\log g$, and $[\text{Fe}/\text{H}]$. A microturbulence velocity of 2 km s^{-1} was adopted for all of the spectra. The line list and atomic data were taken from SPECTRUM⁶. The synthetic spectra have a resolution of 0.01 \AA , covering $4000 \text{ K} \leq T_{\text{eff}} \leq 9000 \text{ K}$ in steps of 250 K, $0.0 \leq \log g \leq 5.0$ in steps of 0.5 dex, and $-4.0 \leq [\text{Fe}/\text{H}] \leq -0.5$ in steps of 0.5 dex. Considering the fact that we are searching for candidate metal-poor stars, the $[\alpha/\text{Fe}]$ was set to +0.4 dex, which is the typical value in this $[\text{Fe}/\text{H}]$ region (e.g., McWilliam 1997).

The second method uses comparisons of line indices. Based on the most up-to-date wavelength definitions of Lick indices⁷, we have calculated corresponding indices for all of the synthetic spectra, resulting in a line index grid covering the corresponding space of stellar parameters. The same series of indices are then calculated for each observed spectrum, and compared with this synthetic grid to find the best match of parameters.

The third method that we adopt is based on a direct comparison of the normalized observed flux with the normalized synthetic spectra in the wavelength range $4500 \text{ \AA} \leq \lambda \leq 5500 \text{ \AA}$.

⁵ See <http://www.lamost.org/public/> for more detailed information, and the progress of the LAMOST surveys.

⁶ <http://www.appstate.edu/~grayro/spectrum/spectrum.html>

⁷ <http://astro.wsu.edu/worthey/html/index.table.html>

TABLE 1
LOG OF THE MAGELLAN/MIKE OBSERVATIONS.

| ID | R.A. | Decl. | r (mag) | Date | Exptime (s) | S/N (pixel ⁻¹) | v_r (km s ⁻¹) |
|-------------------|-------------|-------------|--------------|----------|----------------|-------------------------------|--------------------------------|
| LAMOST J0006+1057 | 00 06 17.20 | +10 57 41.8 | 12.59 | 2013 Dec | 2700 | 86 | -281.6 |
| LAMOST J0102+0428 | 01 02 12.66 | +04 28 24.2 | 10.87 | 2013 Aug | 360 | 72 | -201.3 |
| LAMOST J0126+0135 | 01 26 58.58 | +01 35 15.4 | 12.30 | 2013 Dec | 1800 | 75 | -197.3 |
| LAMOST J0257-0022 | 02 57 06.93 | -00 22 33.7 | 14.97 | 2013 Aug | 1890 | 48 | 2.7 |
| LAMOST J0326+0202 | 03 26 53.88 | +02 02 28.1 | 11.55 | 2013 Dec | 1200 | 106 | 121.2 |
| LAMOST J0343-0227 | 03 43 22.87 | -02 27 56.1 | 13.43 | 2013 Dec | 2400 | 62 | -4.3 |
| LAMOST J1626+1721 | 16 26 14.78 | +17 21 12.1 | 14.29 | 2013 Aug | 1300 | 56 | -177.1 |
| LAMOST J1709+1616 | 17 09 59.79 | +16 16 13.3 | 13.13 | 2013 Aug | 900 | 43 | -324.2 |

NOTE. — The S/N ratio per pixel was measured at $\lambda \sim 4500 \text{ \AA}$.

TABLE 2
EQUIVALENT WIDTH MEASUREMENTS AND LINE-BY-LINE ABUNDANCES.

| Ion | λ (\AA) | χ (eV) | $\log gf$ | J0006+1057 | | | J0102+0428 | | | J0126+0135 | | | J0257-0022 | | |
|------|-------------------------------|----------------|-----------|--------------------------|--------------------|----------|--------------------------|--------------------|----------|--------------------------|--------------------|----------|--------------------------|--------------------|----------|
| | | | | W (m \AA) | $\log \epsilon(X)$ | σ | W (m \AA) | $\log \epsilon(X)$ | σ | W (m \AA) | $\log \epsilon(X)$ | σ | W (m \AA) | $\log \epsilon(X)$ | σ |
| Na I | 5889.95 | 0.00 | 0.108 | 134.7 | 3.05 | 0.09 | 186.1 | 3.69 | 0.09 | 146.3 | 2.86 | 0.11 | ... | ... | ... |
| Na I | 5895.92 | 0.00 | -0.194 | ... | ... | ... | 155.8 | 3.50 | -0.09 | 112.7 | 2.65 | -0.11 | ... | ... | ... |
| Mg I | 3829.35 | 2.71 | -0.208 | ... | ... | ... | 198.4 | 5.36 | 0.12 | 134.0 | 4.38 | -0.07 | 119.7 | 5.30 | -0.17 |
| Mg I | 4167.27 | 4.35 | -0.710 | ... | ... | ... | 52.8 | 5.15 | -0.09 | ... | ... | ... | ... | ... | ... |
| Mg I | 4702.99 | 4.33 | -0.380 | 61.5 | 4.95 | -0.05 | 69.8 | 5.03 | -0.22 | 26.7 | 4.26 | -0.19 | 45.1 | 5.49 | 0.02 |
| Mg I | 5172.68 | 2.71 | -0.450 | ... | ... | ... | 211.2 | 5.36 | 0.12 | 161.7 | 4.49 | 0.04 | 117.1 | 5.40 | -0.07 |
| Mg I | 5183.60 | 2.72 | -0.239 | 187.8 | 5.10 | 0.09 | 230.4 | 5.37 | 0.13 | 178.9 | 4.56 | 0.11 | syn | 5.55 | 0.08 |
| Mg I | 5528.40 | 4.34 | -0.498 | ... | ... | ... | 80.4 | 5.25 | 0.01 | ... | ... | ... | 43.5 | 5.59 | 0.12 |
| Al I | 3943.99 | 0.00 | -0.640 | ... | ... | ... | 154.4 | 3.56 | -0.08 | syn | 2.27 | 0.08 | 60.6 | 3.43 | -0.02 |
| Al I | 3961.52 | 0.01 | -0.340 | 112.5 | 2.61 | 0.05 | 182.4 | 3.72 | 0.08 | syn | 2.12 | -0.08 | 77.3 | 3.46 | 0.02 |
| Si I | 3905.52 | 1.91 | -1.092 | ... | ... | ... | 203.1 | 5.22 | 0.09 | ... | ... | ... | 127.2 | 5.80 | 0.07 |
| Si I | 4102.94 | 1.91 | -3.140 | 61.9 | 4.72 | 0.03 | 85.3 | 5.05 | -0.09 | 61.9 | 4.47 | 0.03 | ... | ... | ... |

NOTE. — The three columns for each objects refer to the measured equivalent width, corresponding abundance in $\log \epsilon(X)$, and the uncertainty caused by the equivalent width measurement. The “syn” indicates that the abundance has been derived using spectral synthesis. (This table is available in its entirety in a machine-readable form.)

The χ^2 minimization technique of Lee et al. (2008) is used to find the best-matching set of parameters.

Taking into account the typical uncertainty of $\sim 0.1 - 0.3$ dex for metallicities derived from low-resolution spectra, an object is regarded as an EMP candidate if it is within the temperature range $4000 \text{ K} < T_{\text{eff}} < 7000 \text{ K}$, and if at least two of the three methods described above yield $[\text{Fe}/\text{H}] \leq -2.7$. The constraint on T_{eff} is adopted to exclude low-luminosity, foreground late-type stars belonging to the disk population(s), and to ensure that only stars rearward of the main-sequence turnoff for stars with ages of ~ 13 Gyr (as predicted by theoretical isochrones) enter the sample. The spectra of the above automatically selected candidates were visually inspected to remove false positives such as cool white dwarfs, or objects that were selected because their spectra were disturbed by reduction artifacts.

2.2. High-resolution Spectroscopy with Magellan/MIKE

For eight of candidates selected as described in Section 2.1, high-resolution spectra were acquired during two runs in 2013 August and 2013 December, with the Magellan Inamori Kyocera Echelle spectrograph (MIKE; Bernstein et al. 2003) at the Magellan-Clay Telescope at Las Campanas Observatory. Among these objects, J0126+0135 and J0326+0202 were previously selected from HES (Frebel et al. 2006), also known as HE 0124-0119 and HE 0324+0152, respectively.

For J0326+0202, high-resolution observation and abundance analysis have been performed as described in Hollek et al. (2011), and we include this object for comparison purpose. For the latter object, J0126+0135, since there has been no high-resolution observation to confirm this object, we have also included it into our target list.

The setup of the observations included a 0:7 slit with 2×2 and 1×2 binning CCD readout modes (used for the two runs respectively), yielding resolving powers of $R \sim 35,000$ in the blue spectral range (3300 — 4900 \AA) and $R \sim 28,000$ in the red spectral range (4900 — 9400 \AA). The spectra have an average signal-to-noise ratio per pixel of $S/N \sim 75$ at 4500 \AA . More information about the observations, as well as the target coordinates and magnitudes, are listed in Table 1.

The raw data were reduced with the standard IRAF⁸ procedures to obtain 1D spectra that are flat-fielded, wavelength-calibrated, co-added, and continuum-normalized. The radial velocities were obtained using the IRAF procedure `fxcor`, employing a synthetic spectrum with low-metallicity as a template.

Equivalent widths were measured by fitting Gaussian pro-

⁸ IRAF is distributed by the National Optical Astronomy Observatory, which is operated by the Association of Universities for Research in Astronomy, Inc., under cooperative agreement with the National Science Foundation.

TABLE 3
ADOPTED STELLAR PARAMETERS OF THE PROGRAM STARS.

| ID | MIKE Measurements | | | | LAMOST Measurement | | |
|-------------------|-------------------------|----------|--------|-------------------------------|-------------------------|----------|--------|
| | T_{eff} (K) | $\log g$ | [Fe/H] | ξ (km^{-1}) | T_{eff} (K) | $\log g$ | [Fe/H] |
| LAMOST J0006+1057 | 4520 | 0.6 | -3.26 | 2.2 | 4800 | 1.6 | -3.03 |
| LAMOST J0102+0428 | 4540 | 0.6 | -2.75 | 2.5 | 4940 | 1.2 | -2.78 |
| LAMOST J0126+0135 | 4330 | 0.1 | -3.57 | 2.8 | 4810 | 1.2 | -3.15 |
| LAMOST J0257-0022 | 6330 | 4.2 | -2.24 | 1.5 | 6260 | 3.6 | -2.65 |
| LAMOST J0326+0202 | 4700 | 1.1 | -3.36 | 1.8 | 4830 | 1.8 | -3.15 |
| LAMOST J0343-0227 | 4790 | 1.5 | -2.42 | 2.0 | 4795 | 1.8 | -2.57 |
| LAMOST J1626+1721 | 5930 | 3.6 | -3.20 | 1.6 | 5830 | 3.4 | -3.00 |
| LAMOST J1709+1616 | 5780 | 3.5 | -3.71 | 1.9 | 6070 | 3.0 | -3.33 |

files to isolated atomic absorption lines based on the line list of Frebel et al. (2013), supplemented with K I, Mn I, and Y II lines from Placco et al. (2014). Table 1 shows the measurements of the adopted atomic lines for all of the program stars. Figure 1 compares our measured equivalent widths of J0326+0202 with those measured by Hollek et al. (2011). There is a mean difference of -0.6 m\AA with $\sigma = 3.4 \text{ m\AA}$ between our measurements and those of Hollek et al. (2011) for lines included in our analysis.

3. STELLAR PARAMETERS AND ABUNDANCE ANALYSIS

For our abundance analysis, we use 1D plane-parallel, hydrostatic model atmospheres of the ATLAS NEWODF grid of Castelli & Kurucz (2003), assuming a mixing-length parameter of $\alpha_{\text{MLT}} = 1.25$, no convective overshooting, and local thermodynamic equilibrium. We use an updated version of the abundance analysis code MOOG (Snedden 1973), which treats continuous scattering as a source function which sums both absorption and scattering rather than true absorption (Sobeck et al. 2011).

We adopt the photospheric Solar abundances of Asplund et al. (2009) when calculating the [X/H] and [X/Fe] abundance ratios.

3.1. Atmospheric Parameters

The effective temperatures T_{eff} of the stars were determined by minimizing the trend of the relationship between the derived abundances and the excitation potentials of Fe I lines. Previous investigations and experience have shown that this procedure yields effective temperatures with systematic offsets compared to those determined from e.g., broadband optical and infrared photometry. Based on a literature sample of metal-poor stars, Frebel et al. (2013) derives a linear relation between the spectroscopic and photometric effective temperatures, and this relation can be used to correct such systematic deviations. Therefore, we have adopted this correction to obtain the final effective temperatures of our sample.

Microturbulent velocities ξ were determined from the analysis of Fe I lines, by forcing the iron abundances of individual lines to exhibit no dependence on the reduced equivalent widths. For objects that have a sufficient number of Fe II lines detected, the surface gravity $\log g$ was determined by minimizing the difference between the average abundances derived from the Fe I and Fe II lines.

However, there are two objects at low metallicities, namely J1626+1721 and J1709+1616, for which only spectra of lower-than-average S/N are available; therefore only one or

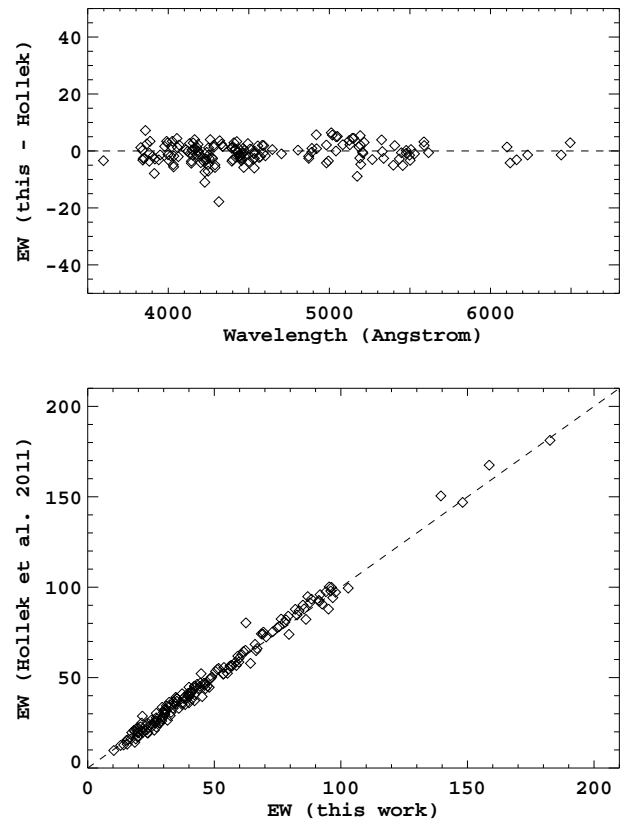


FIG. 1.— Comparison of the equivalent widths of J0326+0202, respectively, measured by this work and Hollek et al. (2011). Top: residuals of the equivalent widths (this work - Hollek) vs. the wavelength. Bottom: direct comparison of the two measurements of the equivalent widths. The one-to-one line is plotted for reference.

no Fe II lines could be detected in their spectra. Therefore, we resorted to the theoretical isochrones of Demarque et al. (2004) to estimate the surface gravities for these objects given their temperatures and metallicities. Isochrones with an age of 13 Gyr were adopted, and all three parameters (i.e., T_{eff} , $\log g$, ξ) were iterated until convergence was reached, i.e., with the derived surface gravity, the “zero” slope can be obtained for derived abundances versus excitation potentials,

and abundances versus EWs, for corresponding T_{eff} and ξ . For these two objects, two solutions of surface gravity could be deduced from the theoretical isochrones for each set of temperature and metallicity, e.g., $\log g$ of 4.57 and 3.62 for J1626+1721, and 4.63 and 3.52 for J1709+1616. However, only the sub-giant $\log g$ value could result in convergence during the iterations, and therefore 3.62 and 3.52 were adopted for J1626+1721 and J1709+1616, respectively.

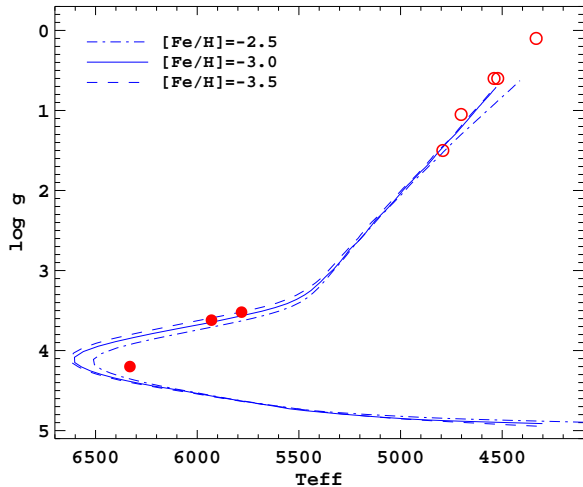


FIG. 2.— T_{eff} vs. $\log g$ of the sample. Filled circles correspond to carbon-enhanced objects, and the open circles refer to the carbon-normal ones, whose definition is described in Section 3.2. For reference, the 13 Gyr theoretical isochrones with $[\alpha/\text{Fe}] = +0.4$ and $[\text{Fe}/\text{H}] = -2.5, -3.0,$ and -3.5 from Demarque et al. (2004) are plotted with dash-dotted, solid and dashed lines respectively.

During the iterations for determining the stellar parameters, any Fe line with an offset of more than 3σ from the mean abundance was rejected. The adopted stellar parameters of all the program stars are listed in Table 1. The derived stellar parameters of J0326+0202 are very close to the values given by Hollek et al. (2011), with a difference of -75 K in T_{eff} , -0.1 in $\log g$, and -0.1 in $[\text{Fe}/\text{H}]$, respectively. The parameters derived from LAMOST low-resolution spectra are also shown, using the average values for the parameters derived from the three methods as described in Section 2.1. A relatively large discrepancy is found in $\log g$ for the cool giants, which is partly due to the large steps (0.5 dex) in $\log g$ of the adopted synthetic spectra template. The general agreement between the two sets of parameters shows that the LAMOST selection pipeline is able to derive reliable parameters, especially T_{eff} and $[\text{Fe}/\text{H}]$. In addition, the $[\text{Fe}/\text{H}]$ derived from LAMOST spectra for J0126+0135 (-3.15) is quite consistent with that from HES follow-up observations (-3.1 , Frebel et al. 2006).

The distribution of T_{eff} versus $\log g$ of all of the program stars is plotted in Figure 2, with filled and open circles referring to the carbon-enhanced and carbon-normal stars in the sample (as will be described in Section 3.2); the theoretical isochrones from Demarque et al. (2004) are also shown for reference.

3.2. Carbon and Nitrogen

The carbon abundances of the program stars were derived by matching the observed CH-AX band head at 4310 \AA (i.e., the G band) to the synthetic spectra. Examples of such fits are

presented in the left panels of Figure 3. The molecular line data for the spectrum synthesis were taken from the Kurucz database.⁹ The line broadening was determined using a single Gaussian profile representing the combined effects from the instrumental profile, atmospheric turbulence, and stellar rotation. The width of the Gaussian was determined by fitting a number of isolated and clear Fe I and Ti II lines whose abundances have been derived from EW measurements.

The nitrogen abundance was measured from the CN-BX electronic transition at 3883 \AA , by comparing the observed spectra with synthetic spectra generated with MOOG (see the right panels of Figure 3 for examples). We could only determine the nitrogen abundances of seven of the program stars whose CN-BX features are strong enough for reliable measurements. We did not use the NH band at 3360 \AA , because of an S/N (typically lower than five) of our spectra at that spectral region that is too low to perform spectral synthesis.

The carbon and nitrogen abundances of the program stars are listed in Table 1.

3.3. Abundances Determined from Atomic Lines

For 19 elements between Na and Ba, the abundances were computed using the measured equivalent widths and the atomic data presented in Table 1, and the stellar parameters in Table 1.

We performed sanity checks for cases where the abundance of an element was derived from a single line, or when abundances deviated by more than 3σ from the average computed for an atomic species from multiple lines. In these cases, the abundances were verified with spectral synthesis and modified if necessary. For clearly detected and isolated lines, synthetic spectra with corresponding abundances derived from the measured equivalent widths could well match the observed spectra. However, for lines that suffer from blending or problems in setting the continuum level, the abundance derived from equivalent widths could not properly match the observed spectral line, and hence the abundance derived from spectral synthesis was adopted. Table 1 lists the used atomic line data, the measured equivalent widths, as well as the derived abundances, where lines marked as “syn” refer to abundances determined with spectral synthesis.

For all of the program stars, the abundances of α elements (Mg, Si, Ca, and Ti) have been determined. Among the light odd-Z elements (Na, Al, K, and Sc), abundances of Sc have been determined for all of the program stars, while for the warmer stars not all the lines are detectable, e.g., the red doublet K lines are too weak in J0257-0022, J1626+1721, and J1709+1616 to derive an abundance. For Fe-peak elements (Cr, Mn, Co, Ni, and Zn), the abundances of Cr and Mn could be determined for all of the program stars; meanwhile the abundances of Co, Ni, and Zn could not be derived for the most metal-deficient object, J1709+1616 due to its low Fe abundance and possibly insufficient S/N. In the cases of the heavy elements (Sr, Y, Ba, and Eu), the abundances of Sr and Ba were determined for all of the program stars except J1709+1616 (the most metal-poor) and J1626+1721, respectively; meanwhile abundances of Y could only be determined for four of these stars, and the Eu lines have been detected and measured in only two objects, J0102+0428, and J0343-0227. All of the elemental abundances of the program stars are shown in Table 1. We have also compared the abundances of

⁹ <http://kurucz.harvard.edu/molecules.html>

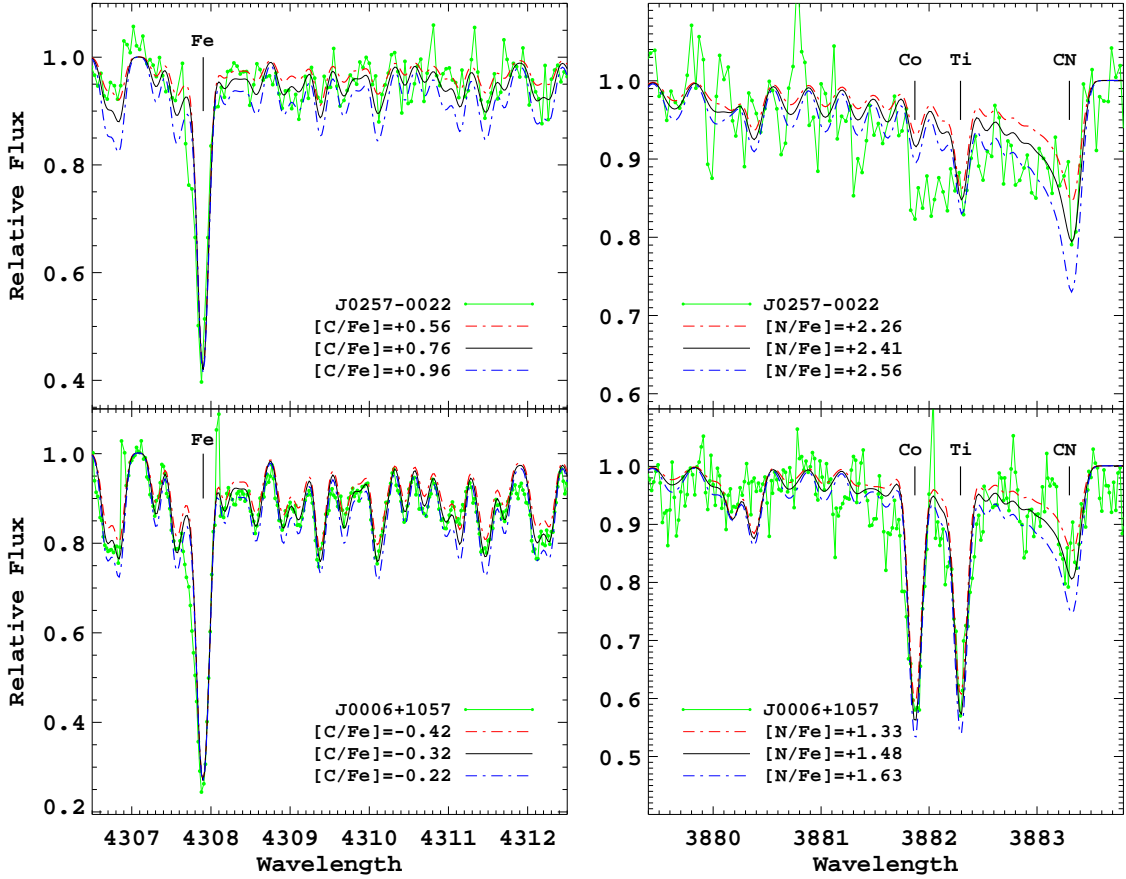


FIG. 3.— Left: examples of fitting of the CH band used to determine the C abundance. Right: examples of fitting of the CN band used to determine the N abundance. The dotted line filled circle represents the observed spectra; the solid line refers to the best fit, and the upper and lower dash-dotted lines correspond to synthetic spectra with changes of 1σ fitting uncertainty in $[C/Fe]$ and $[N/Fe]$. The upper and lower panels refer to the fitting of the spectra of J0257–0022 and J0006+1057, respectively.

J0326+0202 with those from Hollek et al. (2011), as shown in Figure 4. The difference between the abundance from this work and Hollek is -0.14 ± 0.18 , indicating a rather good agreement. The only species with significant difference is Y. Since our measurements have used three Y lines resulting in a standard deviation of 0.08 in the derived abundance, further information should be required to explain the difference.

3.4. Abundance Error Estimation

The error of the derived abundances mainly arises from two aspects, the uncertainties in the equivalent width measurements and those caused by the uncertainties from the stellar parameters.

When $N \geq 2$ lines of individual species of an element were observed, the dispersion in the measurements of multiple lines around the average abundances, i.e., $\sigma \log \epsilon(X)$, was used to present the error caused by random uncertainties in the equivalent widths, as given in Table 1. If the elemental abundance was determined from a single line, the statistic error of the equivalent widths was estimated based on the classical formula of Cayrel (1988):

$$\sigma_{EW} = \langle \Delta W^2 \rangle^{1/2} \simeq 1.6(w\Delta x)^{1/2}\epsilon \quad (1)$$

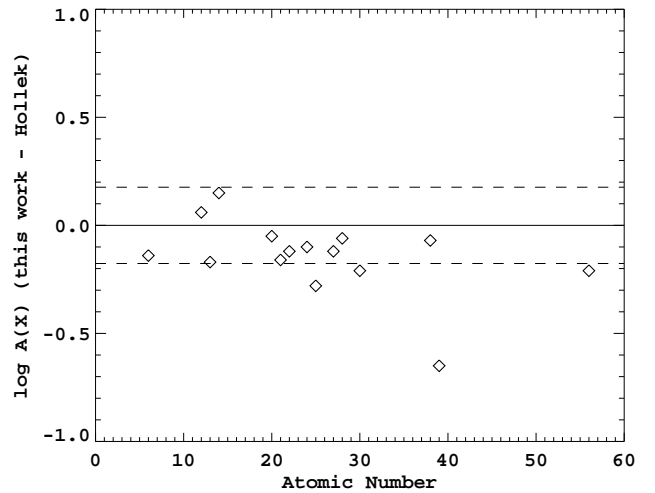


FIG. 4.— Comparison of the abundances of J0326+0202 from this work with the result from Hollek et al. (2011), in the form of the abundance difference vs. the atomic numbers. The dashed lines refer to the standard deviation of the abundance difference (± 0.18). The most deviated point corresponds to the element Y, and is described in the text.

TABLE 4
ABUNDANCES OF INDIVIDUAL ELEMENTS FOR THE PROGRAM STARS.

| | LAMOST J0006+1057 | | | | LAMOST J0102+0428 | | | | LAMOST J0126+0135 | | | | LAMOST J0257-0022 | | | | Sun |
|-------|-------------------|--------|----------|-----|-------------------|--------|----------|-----|-------------------|--------|----------|-----|-------------------|--------|----------|-----|-------------------|
| | log $\epsilon(X)$ | [X/Fe] | σ | N | log $\epsilon(X)$ | [X/Fe] | σ | N | log $\epsilon(X)$ | [X/Fe] | σ | N | log $\epsilon(X)$ | [X/Fe] | σ | N | log $\epsilon(X)$ |
| CH(C) | 4.85 | -0.32 | 0.10 | 1 | 4.75 | -0.93 | 0.15 | 1 | 4.35 | -0.51 | 0.15 | 1 | 6.95 | 0.76 | 0.20 | 1 | 8.43 |
| CN(N) | 6.05 | 1.48 | 0.15 | 1 | 6.45 | 1.37 | 0.15 | 1 | 5.70 | 1.44 | 0.20 | 1 | 8.00 | 2.41 | 0.15 | 1 | 7.83 |
| Na I | 3.05 | 0.07 | 0.09 | 1 | 3.59 | 0.10 | 0.13 | 2 | 2.75 | 0.08 | 0.15 | 2 | ... | ... | ... | ... | 6.24 |
| Mg I | 5.01 | 0.66 | 0.08 | 3 | 5.24 | 0.39 | 0.13 | 7 | 4.45 | 0.42 | 0.13 | 5 | 5.45 | 0.09 | 0.12 | 5 | 7.60 |
| Al I | 2.61 | -0.58 | 0.05 | 1 | 3.64 | -0.06 | 0.11 | 2 | 2.20 | -0.68 | 0.11 | 2 | 3.44 | -0.77 | 0.03 | 2 | 6.45 |
| Si I | 4.72 | 0.47 | 0.03 | 1 | 5.14 | 0.38 | 0.12 | 2 | 4.47 | 0.53 | 0.03 | 1 | 5.80 | 0.53 | 0.07 | 1 | 7.51 |
| K I | 2.51 | 0.74 | 0.01 | 2 | 2.86 | 0.58 | 0.08 | 1 | 2.01 | 0.55 | 0.17 | 1 | ... | ... | ... | ... | 5.03 |
| Ca I | 3.46 | 0.38 | 0.07 | 8 | 3.84 | 0.25 | 0.09 | 18 | 3.21 | 0.44 | 0.09 | 4 | 4.38 | 0.28 | 0.11 | 6 | 6.34 |
| Sc II | -0.09 | 0.02 | 0.07 | 5 | 0.23 | -0.17 | 0.11 | 7 | -0.63 | -0.22 | 0.12 | 5 | 1.04 | 0.13 | 0.05 | 2 | 3.15 |
| Ti I | 1.84 | 0.15 | 0.11 | 6 | 2.19 | -0.01 | 0.12 | 21 | 1.74 | 0.36 | 0.14 | 3 | 3.32 | 0.61 | 0.19 | 2 | 4.95 |
| Ti II | 1.87 | 0.18 | 0.12 | 12 | 2.27 | 0.07 | 0.14 | 45 | 1.35 | -0.03 | 0.18 | 16 | 3.18 | 0.47 | 0.10 | 15 | 4.95 |
| V II | 0.96 | 0.29 | 0.04 | 1 | 1.22 | 0.04 | 0.12 | 3 | 0.60 | 0.24 | 0.04 | 1 | ... | ... | ... | ... | 3.93 |
| Cr I | 1.91 | -0.47 | 0.16 | 5 | 2.65 | -0.24 | 0.14 | 15 | 1.43 | -0.64 | 0.14 | 6 | 3.18 | -0.22 | 0.08 | 3 | 5.64 |
| Cr II | ... | ... | ... | ... | 3.09 | 0.20 | 0.07 | 1 | ... | ... | ... | ... | ... | ... | ... | ... | 5.64 |
| Mn I | 1.67 | -0.50 | 0.11 | 4 | 2.12 | -0.56 | 0.12 | 5 | 0.86 | -1.00 | 0.06 | 3 | 2.65 | -0.54 | 0.09 | 3 | 5.43 |
| Fe I | 4.24 | 0.00 | 0.14 | 94 | 4.75 | 0.00 | 0.15 | 164 | 3.93 | 0.00 | 0.19 | 61 | 5.26 | 0.00 | 0.14 | 60 | 7.50 |
| Fe II | 4.24 | 0.00 | 0.13 | 11 | 4.76 | 0.01 | 0.10 | 19 | 3.93 | 0.00 | 0.15 | 4 | 5.25 | -0.01 | 0.14 | 3 | 7.50 |
| Co I | 1.87 | 0.14 | 0.04 | 1 | 2.13 | -0.11 | 0.16 | 7 | 1.59 | 0.17 | 0.01 | 2 | 3.03 | 0.28 | 0.12 | 1 | 4.99 |
| Ni I | 2.90 | -0.06 | 0.06 | 3 | 3.25 | -0.22 | 0.18 | 6 | 2.57 | -0.08 | 0.07 | 1 | 4.07 | 0.09 | 0.12 | 2 | 6.22 |
| Zn I | 1.72 | 0.42 | 0.04 | 2 | 1.80 | -0.01 | 0.10 | 1 | 1.43 | 0.44 | 0.07 | 2 | 2.71 | 0.39 | 0.14 | 1 | 4.56 |
| Sr II | -2.46 | -2.07 | 0.06 | 2 | -1.06 | -1.18 | 0.14 | 2 | -2.31 | -1.61 | 0.04 | 1 | 1.05 | 0.42 | 0.12 | 2 | 2.87 |
| Y II | ... | ... | ... | ... | -1.62 | -1.08 | 0.03 | 3 | ... | ... | ... | ... | -0.08 | -0.05 | 0.11 | 1 | 2.21 |
| Ba II | -2.83 | -1.75 | 0.03 | 1 | -1.26 | -0.69 | 0.13 | 5 | -2.53 | -1.14 | 0.16 | 3 | -0.17 | -0.11 | 0.00 | 2 | 2.18 |
| Eu II | ... | ... | ... | ... | -2.13 | 0.10 | 0.08 | 1 | ... | ... | ... | ... | ... | ... | ... | ... | 0.52 |

TABLE 4
CONTINUED.

| | LAMOST J0326+0202 | | | | LAMOST J0343-0227 | | | | LAMOST J1626+1721 | | | | LAMOST J1709+1616 | | | | Sun |
|-------|-------------------|--------|----------|-----|-------------------|--------|----------|-----|-------------------|--------|----------|-----|-------------------|--------|----------|-----|-------------------|
| | log $\epsilon(X)$ | [X/Fe] | σ | N | log $\epsilon(X)$ | [X/Fe] | σ | N | log $\epsilon(X)$ | [X/Fe] | σ | N | log $\epsilon(X)$ | [X/Fe] | σ | N | log $\epsilon(X)$ |
| CH(C) | 5.15 | 0.08 | 0.10 | 1 | 5.90 | -0.11 | 0.15 | 1 | 6.30 | 1.07 | 0.20 | 1 | 6.30 | 1.58 | 0.20 | 1 | 8.43 |
| CN(N) | 5.70 | 1.23 | 0.15 | 1 | 6.35 | 0.94 | 0.15 | 1 | ... | ... | ... | ... | ... | ... | ... | ... | 7.83 |
| Na I | 3.46 | 0.58 | 0.01 | 2 | 3.26 | -0.02 | 0.14 | 2 | 3.02 | -0.02 | 0.03 | 2 | ... | ... | ... | ... | 6.24 |
| Mg I | 4.99 | 0.75 | 0.17 | 8 | 5.58 | 0.40 | 0.03 | 4 | 4.90 | 0.50 | 0.16 | 3 | 4.17 | 0.28 | 0.12 | 3 | 7.60 |
| Al I | 2.36 | -0.73 | 0.04 | 1 | 3.50 | -0.53 | 0.06 | 1 | 2.92 | -0.33 | 0.08 | 1 | ... | ... | ... | ... | 6.45 |
| Si I | 4.93 | 0.78 | 0.07 | 2 | 5.52 | 0.43 | 0.04 | 1 | 4.77 | 0.46 | 0.09 | 1 | 3.98 | 0.18 | 0.10 | 1 | 7.51 |
| K I | 2.49 | 0.82 | 0.03 | 2 | 3.12 | 0.51 | 0.08 | 1 | ... | ... | ... | ... | ... | ... | ... | ... | 5.03 |
| Ca I | 3.40 | 0.42 | 0.08 | 12 | 4.23 | 0.31 | 0.11 | 14 | 3.41 | 0.27 | 0.08 | 2 | 3.05 | 0.42 | 0.11 | 1 | 6.34 |
| Sc II | -0.23 | -0.02 | 0.04 | 5 | 0.65 | -0.08 | 0.07 | 5 | 0.02 | 0.07 | 0.11 | 1 | -0.37 | 0.19 | 0.14 | 1 | 3.15 |
| Ti I | 1.81 | 0.22 | 0.06 | 7 | 2.70 | 0.17 | 0.11 | 15 | ... | ... | ... | ... | ... | ... | ... | ... | 4.95 |
| Ti II | 1.75 | 0.16 | 0.10 | 32 | 2.79 | 0.26 | 0.11 | 27 | 1.92 | 0.17 | 0.11 | 11 | 1.90 | 0.66 | 0.13 | 10 | 4.95 |
| V II | 0.60 | 0.03 | 0.03 | 1 | 1.52 | 0.01 | 0.05 | 1 | ... | ... | ... | ... | ... | ... | ... | ... | 3.93 |
| Cr I | 1.92 | -0.36 | 0.16 | 6 | 3.00 | -0.22 | 0.08 | 9 | 2.19 | -0.25 | 0.06 | 3 | 1.64 | -0.29 | 0.15 | 1 | 5.64 |
| Cr II | ... | ... | ... | ... | 3.31 | 0.09 | 0.06 | 1 | ... | ... | ... | ... | ... | ... | ... | ... | 5.64 |
| Mn I | 1.42 | -0.65 | 0.09 | 3 | 2.80 | -0.21 | 0.09 | 6 | 2.04 | -0.19 | 0.10 | 1 | 1.65 | -0.07 | 0.11 | 1 | 5.43 |
| Fe I | 4.14 | 0.00 | 0.10 | 127 | 5.08 | 0.00 | 0.13 | 111 | 4.30 | 0.00 | 0.13 | 46 | 3.79 | 0.00 | 0.14 | 24 | 7.50 |
| Fe II | 4.13 | -0.01 | 0.11 | 7 | 5.08 | 0.00 | 0.15 | 14 | ... | ... | ... | ... | ... | ... | ... | ... | 7.50 |
| Co I | 1.82 | 0.19 | 0.10 | 5 | 2.60 | 0.03 | 0.07 | 2 | 2.42 | 0.63 | 0.10 | 1 | ... | ... | ... | ... | 4.99 |
| Ni I | 2.89 | 0.03 | 0.09 | 5 | 3.90 | 0.10 | 0.09 | 7 | 3.19 | 0.17 | 0.14 | 2 | ... | ... | ... | ... | 6.22 |
| Zn I | 1.42 | 0.22 | 0.04 | 2 | 2.35 | 0.21 | 0.06 | 1 | ... | ... | ... | ... | ... | ... | ... | ... | 4.56 |
| Sr II | -1.18 | -0.69 | 0.01 | 2 | 0.29 | -0.16 | 0.07 | 2 | -0.84 | -0.51 | 0.03 | 2 | ... | ... | ... | ... | 2.87 |
| Y II | -1.98 | -0.83 | 0.08 | 3 | -0.58 | -0.37 | 0.09 | 4 | ... | ... | ... | ... | ... | ... | ... | ... | 2.21 |
| Ba II | -2.55 | -1.37 | 0.03 | 2 | -0.58 | -0.34 | 0.18 | 4 | ... | ... | ... | ... | -1.54 | -0.01 | 0.18 | 1 | 2.18 |
| Eu II | ... | ... | ... | ... | -1.99 | -0.09 | 0.04 | 2 | ... | ... | ... | ... | ... | ... | ... | ... | 0.52 |

NOTE. — The column of “ N ” refers to the number of lines adopted for determination of the elemental abundances. The photospheric solar abundances from Asplund et al. (2009) are also shown for reference.

TABLE 5
UNCERTAINTIES OF $\log \epsilon(X)$ PROPAGATED FROM THE
STELLAR PARAMETERS (AS DESCRIBED IN SECTION 3.4),
COMPUTED FOR J0326+0202 AS AN EXAMPLE.

| Ion | ΔT_{eff} + 150 K | $\Delta \log g$ + 0.3 dex | $\Delta \xi$ + 0.3 km s ⁻¹ | σ_{tot} |
|-------|------------------------------------|------------------------------|--|-----------------------|
| CH(C) | 0.30 | -0.15 | -0.05 | 0.34 |
| CN(N) | 0.25 | -0.05 | 0.00 | 0.25 |
| Na I | 0.17 | -0.03 | -0.18 | 0.25 |
| Mg I | 0.13 | -0.06 | -0.08 | 0.16 |
| Al I | 0.15 | -0.05 | -0.18 | 0.24 |
| Si I | 0.16 | -0.02 | -0.03 | 0.16 |
| K I | 0.12 | -0.02 | -0.02 | 0.12 |
| Ca I | 0.11 | -0.03 | -0.04 | 0.12 |
| Sc II | 0.10 | 0.08 | -0.08 | 0.15 |
| Ti I | 0.19 | -0.03 | -0.02 | 0.19 |
| Ti II | 0.08 | 0.08 | -0.08 | 0.14 |
| V II | 0.08 | 0.09 | -0.01 | 0.12 |
| Cr II | 0.18 | -0.04 | -0.09 | 0.21 |
| Mn I | 0.21 | -0.05 | -0.14 | 0.26 |
| Fe I | 0.17 | -0.04 | -0.10 | 0.20 |
| Fe II | 0.02 | 0.09 | -0.06 | 0.11 |
| Co I | 0.21 | -0.03 | -0.07 | 0.22 |
| Ni I | 0.20 | -0.05 | -0.20 | 0.29 |
| Zn I | 0.09 | 0.04 | 0.01 | 0.10 |
| Sr II | 0.11 | 0.07 | -0.27 | 0.30 |
| Y II | 0.13 | 0.08 | -0.01 | 0.15 |
| Ba II | 0.14 | 0.08 | -0.03 | 0.16 |

where w is the FWHM of the line, Δx refers to the sampling step of the MIKE spectra, and ϵ refers to the reciprocal spectral S/N in the case of normalized spectra. The uncertainty in the derived abundance corresponding to $2\sigma_{EW}$ was adopted as a conservative estimate of the random error caused by the equivalent width measurement. The errors relevant to the uncertainties of the equivalent width measurement are listed in Table 1 for each individual line that has been used for abundance estimation.

The abundance uncertainties associated with the uncertainties of the stellar parameters were estimated by varying T_{eff} by +150 K, $\log g$ by +0.3 dex, and ξ by +0.3 km s⁻¹ in the stellar atmospheric model. Table 1 summarizes the corresponding abundance uncertainties and the total uncertainty for the three errors, which was computed as the quadratic sum, for J0326+0202 as an example. We noted that the abundance uncertainties caused by the equivalent width measurements are generally smaller than those propagating from the stellar parameters, and therefore, we have adopted the latter uncertainties as reference error bars for further discussions concerning the abundances of the sample.

4. RESULTS AND INTERPRETATION

4.1. CEMP and NEMP Objects

Despite the limited sample size, there are several objects in our sample exhibiting relatively high [C/Fe] ratios, as shown in Figure 5. To check the fraction of CEMP stars, we have adopted the classification of Aoki et al. (2007), who suggest a scheme that takes into consideration the nucleosynthesis and mixing effects in giants. This is important for our sample, because five of our nine stars are giants (see Figure 2). We therefore consider a star to be CEMP when $[C/Fe] \geq +0.7$ in the case of stars with luminosities of $\log(L/L_{\odot}) \leq 2.3$, or when $[C/Fe] \geq +3.0 - \log(L/L_{\odot})$ in the case of stars with $\log(L/L_{\odot}) > 2.3$. The luminosities of our sample stars were computed based on the prescription of Aoki et al. (2007), as-

suming a typical mass of $M = 0.8M_{\odot}$ for halo stars.

Figure 5a shows that there are four objects in our sample that are above the limit, among which there is a red giant J0126+0135 that is located slightly off the limit and has very low $[C/Fe] = -0.51$. Therefore, we have decided to classify only the three objects with $[C/Fe] > 0.7$ as CEMP stars (filled circles in Figure 5) and the rest as carbon-normal objects (open circles).

It is known that in addition to [C/Fe], [N/Fe] is notably enhanced in many CEMP stars as well, and although this phenomenon appears to be rare, a population of nitrogen-enhanced metal-poor (NEMP) stars with $[N/C] > 0.5$ has been discovered (Johnson et al. 2007; Pols et al. 2012). We have adopted the criteria of Pols et al. (2012) for classifying stars as NEMP, i.e., $[N/Fe] \geq 1.0$ and $[N/C] \geq 0.5$. In Figure 5(b), it can be seen that among the six program stars with determined nitrogen abundances, there are five that are on the right side of the dotted line, and hence are nitrogen-enhanced. However, as can be seen in Figure 2 and of Figure 5(a), four of them have $[C/Fe] \lesssim 0.0$ and $[N/Fe]$ between 1.2 through 1.5, and are on the upper part of the red giant branch, and thus they may not be genuine NEMP, as will be discussed in Section 4.5.

If we use the separation of so-called “mixed” from “unmixed” stars defined as in Spite et al. (2005) (i.e., the dashed line in Figure 5(b), corresponding to $[N/Fe] = 0.5$), the four objects belong to the group of “mixed” stars. In these stars, nitrogen has been produced from the burning of carbon, and hence they are usually carbon-poor and nitrogen-rich. The same holds true when the alternative criterion of Pols et al. (2012) of $[(C+N)/Fe] > 0.9$ is considered (the dash-dotted line in Figure 5(b)). The CEMP turn-off star J0257-0022 is well located in the NEMP region, which makes it a potential carbon and nitrogen-enhanced metal-poor (CNEMP) star (Pols et al. 2012). We will further discuss this point in Section 4.5.

4.2. Abundance Trends of the Light Elements

The abundance ratios $[X/Fe]$ of the program stars are plotted against $[Fe/H]$ in the right panels of Figure 6 for the elements from C through Zn. The observed chemical abundances of metal-poor stars from the “First Stars” program (Cayrel et al. 2004), and from Yong et al. (2013a) and Placco et al. (2014), are also plotted for comparison. Note that the “First Stars” sample has been re-analyzed by Yong et al. (2013a), but since there are a few elements not included in their analysis, we have adopted the abundances of the sample of “First Stars” from Cayrel et al. (2004), Spite et al. (2005), and François et al. (2007).

In general, the abundance ratios seen in our sample agree well with the abundance ratio trends defined by the literature samples. However, for the most iron-deficient object in our sample (J1709+1616), and the carbon and nitrogen-enhanced object J0257-0022, a few elements (in particular, Ti, Mn, and Ba) show slight deviations from these trends.

Compared with those of other elements, dispersions in the distributions of C, N, Na, and Al are notably larger. Unlike the behavior found by Yong et al. (2013a), the abundance ratios of the α elements Mg and Si (as well as Ca) of the program stars distribute around the typical halo value of $[\alpha/Fe] = 0.4$ (e.g., McWilliam 1997, the dotted lines in Figure 6).

Among the iron-peak elements, a small scatter and clear dependence on Fe are found for Cr and Zn. The abundance ratio of [Cr/Fe] exhibits the lowest observed scatter together

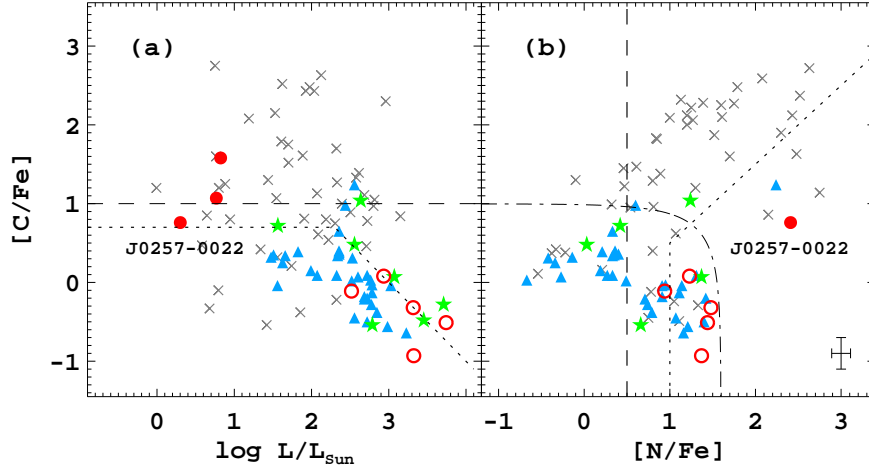


FIG. 5.— (a) $[C/Fe]$ ratio as a function of the luminosity estimated from T_{eff} and $\log g$ of our sample. The dotted line indicates the dividing line between carbon-enhanced and carbon-normal stars as defined in Aoki et al. (2007). The dashed line corresponds to $[C/Fe] = 1.0$. (b) $[C/Fe]$ vs. $[N/Fe]$. The two criteria for NEMP stars suggested by Pols et al. (2012) are respectively shown in dashed ($[N/Fe] \geq 1.0$ and $[N/C] \geq 0.5$) and dash-dotted lines ($[(C+N)/Fe] > 0.9$). The filled and open circles respectively refer to carbon-enhanced and carbon-normal stars. Metal-poor stars from “First Stars” (Spite et al. 2005), Yong et al. (2013a), and Placco et al. (2014) are also plotted for comparison, in filled triangles, crosses, and filled pentacles, respectively. The potential CNEMP object J0257–0022 is marked.

with a positive slope, which agrees well with the results of Cayrel et al. (2004). These authors interpreted this trend as an indication that Cr and Fe are produced in the same nucleosynthesis process, so that mixing in the interstellar medium would not result in any significant scatter around the abundance trend. Furthermore, a clear anti-correlation between $[Zn/Fe]$ and $[Fe/H]$ is seen. This suggests that neutron-capture processes may not have contributed much to the production of Zn in progenitors of these EMP stars, since if that is the case, an anti-correlation versus metallicities would be expected for the abundance ratio.

4.3. Neutron-capture Elements

The abundance ratios of the neutron-capture elements Sr, Y, Ba, and Eu versus $[Fe/H]$ are shown in Figure 7. In agreement with previous investigations, very large dispersions are seen, especially at $[Fe/H] < -2.8$ (Ryan et al. 1996; Cayrel et al. 2004). For all of the program stars with measurable Ba abundances, the $[Ba/Fe]$ ratios are not higher than the Solar value, which means that these two carbon-enhanced stars (J0257–0022 and J1709+1616) belong to the class of CEMP-no stars. Eu abundances are only measured in the two giants with relatively higher metallicities. Both giants show a near-Solar abundance ratio of $[Eu/Fe]$, and combined with the “First Stars” sample support the indication that metal-poor stars with high $[Eu/Fe]$ are rare (François et al. 2007).

The abundance ratios of neutron-capture elements such as $[Sr/Ba]$ can be used to investigate the possible nucleosynthesis processes that have occurred in the progenitors of EMP stars. Aoki et al. (2013) has found several remarkable features in the distribution of $[Sr/Ba]$ versus $[Fe/H]$, including a cutoff at approximately $[Fe/H] \sim -3.6$, and a lower bound at about $[Sr/Ba] \sim -0.5$. Figure 8(a) shows the distribution of $[Sr/Ba]$ for our program stars and the metal-poor star samples from the literature as a function of $[Fe/H]$. As can be seen, the number of observed objects is indeed very limited around $[Sr/Ba] \sim -0.5$ and below. However, from the currently available data set of metal-poor stars, it does not seem clear whether the cutoff at $[Fe/H] < -3.6$ actually exists. It is possible that there may be a cutoff or sharp drop of the dis-

tribution of objects with $[Sr/Ba]$ larger than the Solar value at even lower metallicities, but this would require a larger body of data for EMP and UMP stars for further exploration.

Figure 8(b) shows that if we adopt Ba as a reference element, a major trend of anti-correlation between $[Sr/Ba]$ and $[Ba/H]$ can be found all the way down to $[Ba/H] \sim -4.5$, while the abundance ratio reverts back to a nearly Solar value when it approaches to lower $[Ba/H]$. This is quite agreeable with the results of François et al. (2007), and we suspect that the anti-correlation may extend to $[Ba/H]$ higher than -1.5 , e.g., to around $[Ba/H] \sim 0.0$. The observed distribution trend of $[Sr/Ba]$ against $[Ba/H]$ indicates that besides the main rapid neutron-capture process, it is likely that an additional nucleosynthesis mechanism such as a second neutron-capture process has contributed to the observed amounts of Sr (and other neutron-capture elements) at $[Ba/H] > -4.5$ (e.g., Wanajo et al. 2001; Travaglio et al. 2004; Qian & Wasserburg 2007).

4.4. Abundance Patterns and Chemical Peculiarities

Despite the observed diversity in chemistry among low-metallicity stars, based on homogeneously analyzed samples of metal-poor stars (Cayrel et al. 2004; Yong et al. 2013a) it is believed that there exists a population that conforms to the average abundance pattern, and thus is regarded as the chemically “normal” population. Considering the fact that most of the carbon-normal objects in our sample are giants, we have adopted the coefficients of the regression fit of Cayrel et al. (2004), which were determined by means of a sample of metal-poor giants for which very high-quality spectra were obtained. The results of our comparison of the abundance patterns are shown in Figure 9. For an element between Na and Zn, if the $[X/Fe]$ ratio deviates more than 0.5 dex from the reference abundance pattern, it is regarded as abnormal and marked by filled squares. For five out of the eight program stars, there is at least one element showing such an abnormal abundance. However, if only carbon-normal objects with more than one abnormal element are counted, only J0326+0202 exhibits a moderate over-abundance in Na and Mg.

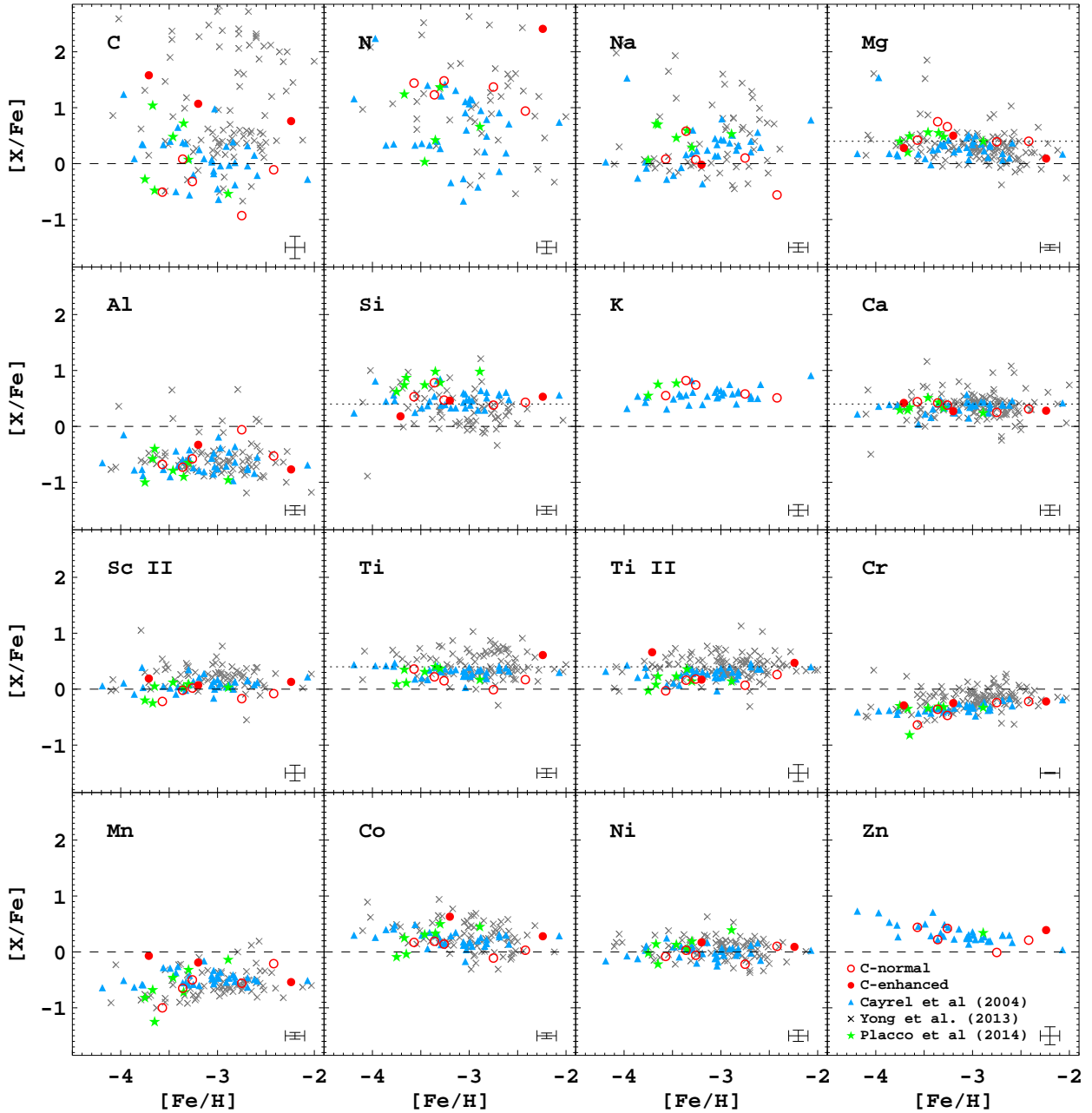


FIG. 6.— $[X/Fe]$ vs. $[Fe/H]$ of 15 elements (16 species) lighter than Zn. For all α elements (Mg, Si, Ca, and Ti), the canonical value of $[\alpha/Fe] \sim +0.4$ for the halo stars (McWilliam 1997) is plotted for reference. The meanings of the different symbols are the same as in Figure 5.

Regarding neutron-capture elements, none of our stars are strongly enhanced in Sr, Y, Ba, or Eu relative to the Solar abundance ratios. However, we note that two of our stars, J0006+1057 and J0126+0135, have quite low Sr and Ba abundances, respectively with $[Sr/H]$ of -5.33 and -5.18 , and $[Ba/H]$ of -5.01 and -4.71 . Using the stellar abundance data of over 1,000 stars from the Galactic field and dwarf galaxies, Roederer (2013) has noted that strontium and barium have been detected in all environments. When comparing J0006+1057 and J0126+0135 with Roederer (2013)’s Figure 1 which presents the distribution of $[Ba/H]$ versus $[Sr/H]$ in field stars and dwarf galaxies, both of our program stars are located in the lower left corner of the plot, and close to the detection thresholds. As pointed out by Roederer (2013), such objects with unusually low $[Sr/H]$ and $[Ba/H]$ are of

great interest, in the sense that they raise the prospect that at the early phase of Galactic chemical evolution there is at least one kind of neutron-capture processes operating as frequently as the nucleosynthesis mechanisms that produce lighter elements such as α and iron-peak elements. Interestingly, J0006-1057 and J0126+0135 have $[Sr/Ba]$ ratios of -0.3 and -0.5 , respectively (see Table 1 and the right panel of Figure 8). These values very much resemble those seen in strongly r -process-enhanced stars, such as CS22892-052 ($[Sr/Ba] = -0.4$; Sneden et al. 2003), rather than the values typical for stars showing the abundance signature of the weak r -process, e.g., HD122563 ($[Sr/Ba] = +0.8$; Honda et al. 2006). This suggests that not only the weak r -process, but also the main r -process contributed significantly to the inventory of neutron-capture elements during the earliest phases of

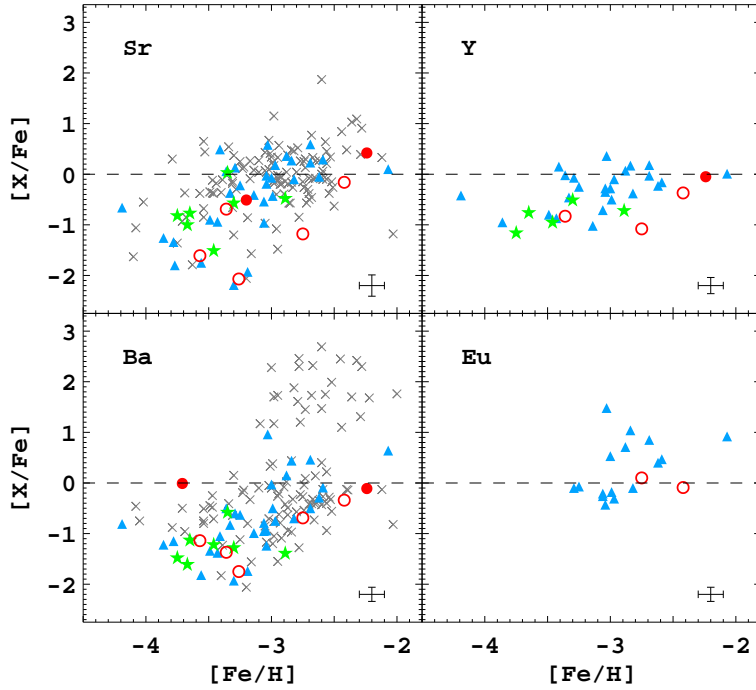


FIG. 7.— $[\text{Sr}/\text{Fe}]$, $[\text{Y}/\text{Fe}]$, $[\text{Ba}/\text{Fe}]$ and $[\text{Eu}/\text{Fe}]$ vs. $[\text{Fe}/\text{H}]$ of the program stars. The meanings of the different symbols are the same as in Figure 5, except that the triangles refer to data from François et al. (2007).

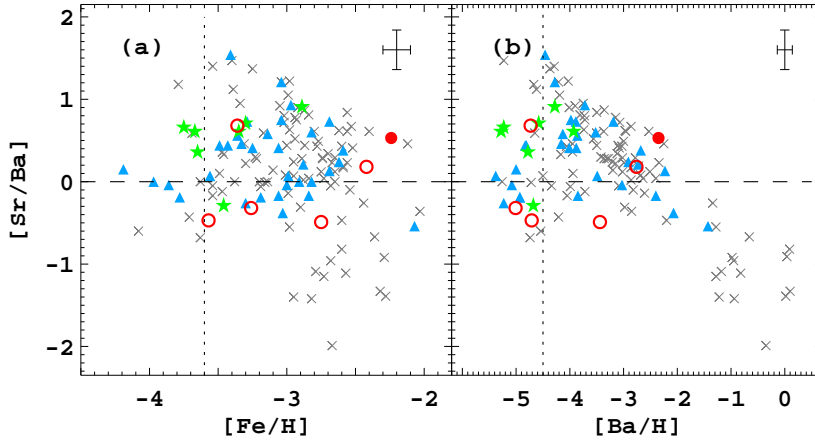


FIG. 8.— $[\text{Sr}/\text{Ba}]$ vs. $[\text{Fe}/\text{H}]$ (a) and $[\text{Ba}/\text{H}]$ (b) of the program stars. The meaning of different symbols are the same as in Figure 7. The horizontal dash-dotted lines refer to $[\text{Sr}/\text{Ba}] \sim \pm 0.4$, as guidance of the abundance range to identify the weak and main r -processes. The vertical dotted lines correspond to $[\text{Fe}/\text{H}] = -3.6$ and $[\text{Ba}/\text{H}] = -4.5$ in the two panels, respectively.

Galactic chemical evolution.

Given the fact that Yong et al. (2013a) found only seven chemically peculiar objects in a sample of more than 100 carbon-normal stars, the abundance patterns of our sample confirm that a chemically “normal” population does exist among metal-poor stars which may dominate, the low-metallicity region even at $[\text{Fe}/\text{H}] < -3.7$.

4.5. “Mixed” or “Unmixed”?

Spite et al. (2005) observed a separation at $[\text{C}/\text{N}] \sim -0.6$ among 35 EMP giants, and adopted such a separation to divide their sample into “mixed” and “unmixed” groups. Because the CNO process turns carbon into nitrogen, the $[\text{C}/\text{N}]$

ratio is believed to be a sensitive indicator of mixing; the observed separation demonstrates the signature of CN-cycle processing in the surface abundances of these halo giants. We thus compare the $[\text{C}/\text{N}]$ abundance ratio of our stars for objects with both measurements of carbon and nitrogen in the samples of Spite et al. (2005), Yong et al. (2013a), and Placco et al. (2014).

As shown in Figure 10a, for the carbon-normal stars, i.e., the majority of the sample from Spite et al. (2005, filled triangles), Placco et al. (2014, filled stars), and our program stars (open circles), there are two distinct groups of stars that can be separated by the dividing line at $[\text{C}/\text{N}] \sim -0.6$. We also note that there are very few carbon-enhanced objects (the major-

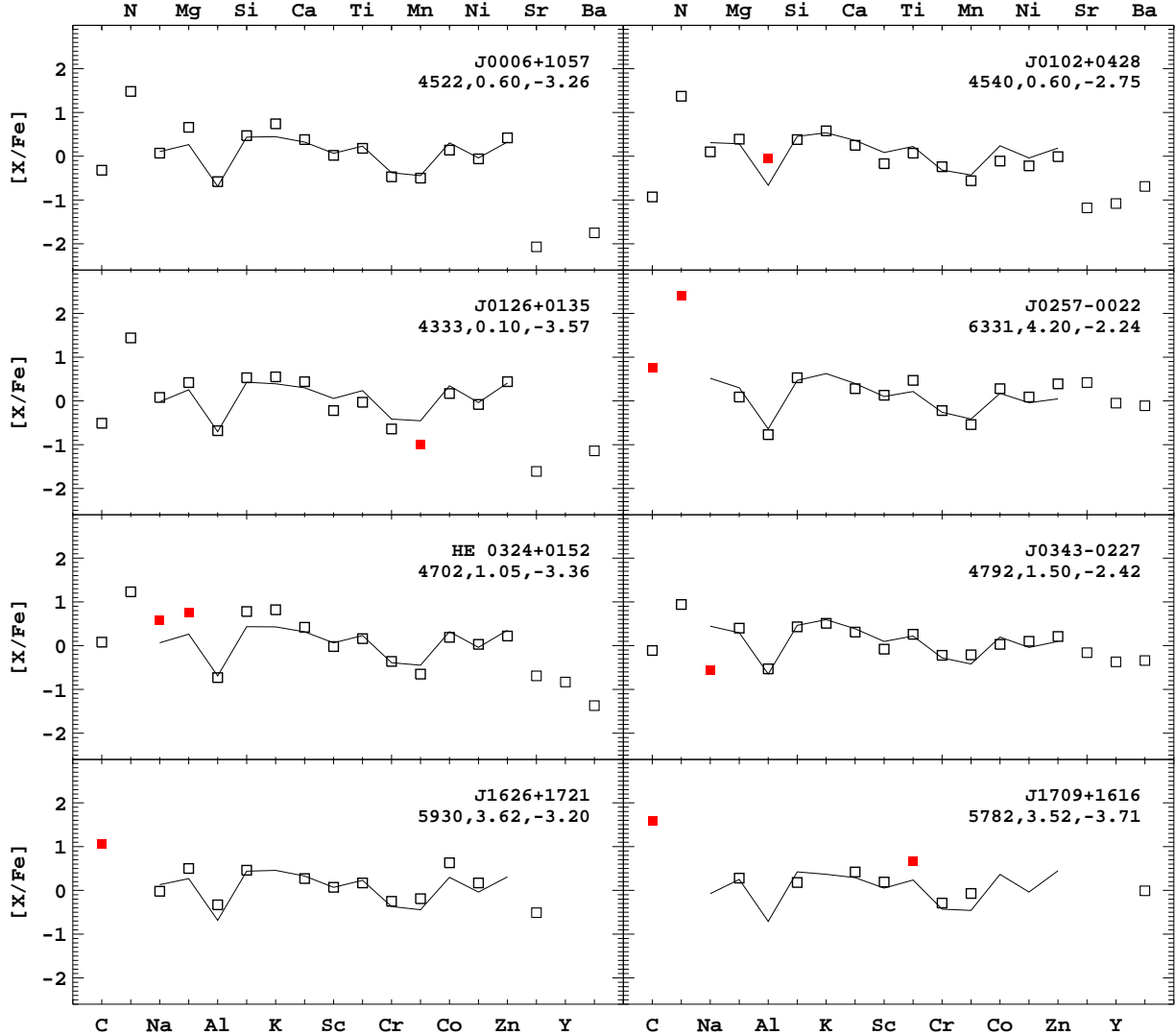


Fig. 9.— Abundance pattern of the program stars. The solid line represents the “average” abundance derived from the regression coefficients from Cayrel et al. (2004). Filled squares refer to enhancement in carbon and/or nitrogen as defined in Section 4.1, and elements with an abundance that differs from the solid line by more than 0.5 dex. The derived T_{eff} , $\log g$, and $[\text{Fe}/\text{H}]$ together with the ID of each object are listed in the plot.

ity of the Yong et al. 2013a sample and J0257–0022) below the dividing line. This could be due to the fact that a great many of them are significantly enhanced in carbon, and/or are main-sequence turnoff stars or dwarfs (as can be seen in Figure 10(b) and Figure 10(c)) whose deeper layers have not yet been dredged-up.

However, we note that the potential CNEMP turn-off star of our sample, J0257–0022, lies well below the dividing line along with the “mixed” group. This is rather interesting, since for this object the material processed in the CN cycle has presumably not yet been dredged up from its interior to the outer layer. For comparison, two unevolved NEMP candidates from Pols et al. (2012), HE 1337+0012, and HD 25329 are also plotted in Figure 10. Despite the different carbon abundances of these objects, they are in a quite similar situation to J0257–0022, e.g., unevolved (dwarf or main-sequence turnoff), nitrogen-enhanced, and located in/close to the region of the “mixed” group. As indicated in Pols et al. (2012), “genuine” NEMP stars are supposed to show signatures of

accretion of material that has undergone hot bottom burning (HBB), e.g., large enhancement in sodium and magnesium, while heavy s -process elements such as barium and lead should not be significantly enhanced. The low sodium abundance ($[\text{Na}/\text{Fe}] = -1.13$, Aoki et al. 2006) of HE 1337+0012 basically rules out the possibility of accretion from HBB. For HD 25329, only slight enhancements in sodium and magnesium are shown ($[\text{Na}/\text{Fe}] = +0.24$, and $[\text{Mg}/\text{Fe}] = +0.59$, Gratton et al. 2003), which does not support the material being accreted from an HBB process either. For J0257–0022, a lack of enhancement in magnesium ($[\text{Mg}/\text{Fe}] = +0.09$) and no measurable sodium lines make it very unlikely to be enriched by the accreted material from the HBB. However, the origin of the nitrogen-enhanced status of these unevolved stars will remain unclear until more detailed abundance analysis is available.

5. CONCLUSIONS

Eight potential metal-poor stars have been selected from DR1 of the low-resolution spectroscopic survey of LAMOST

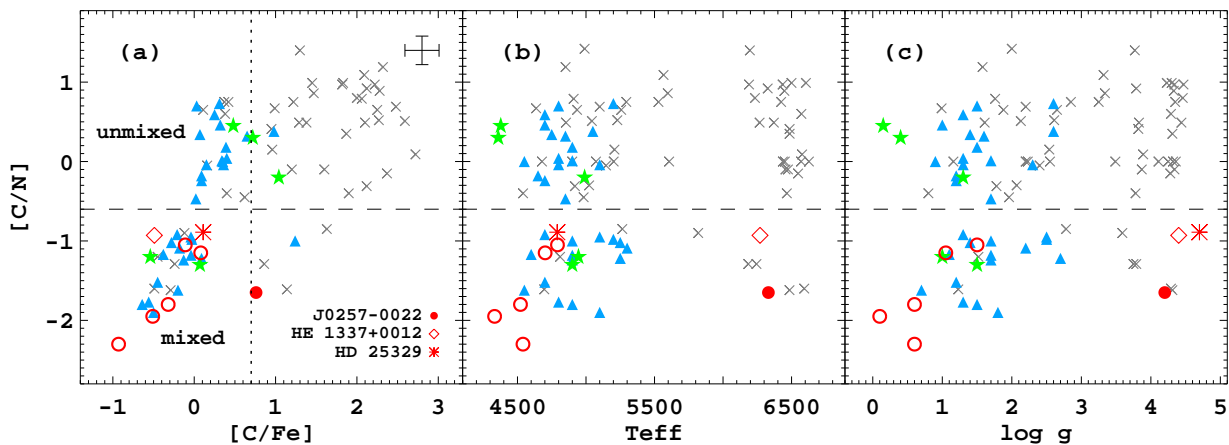


FIG. 10.— (a) $[C/N]$ vs. $[C/Fe]$, (b) $[C/N]$ vs. T_{eff} , and (c) $[C/N]$ vs. $\log g$ for the sample. The plots only include objects with both measured abundances of carbon and nitrogen. The dashed lines in all plots refer to $[C/N] = -0.6$ which is used by Spite et al. (2005) to separate the mixed and unmixed stars. The dotted lines in frame (a) refer to the adopted division of carbon-normal and carbon-rich stars, i.e., $[C/Fe] = 0.7$, as described in the text. The potential CNEMP object J0257–0022 (filled circle) is marked, together with two other unevolved NEMP candidates, HE 1337+0012 (diamond) and HD 25329 (star) from Pols et al. (2012). The meanings of the other symbols are the same as in Figure 5.

and follow-up observations in high-resolution spectroscopy with Magellan/MIKE. Based on the high-resolution analysis, we have confirmed five EMP stars, including two with $[Fe/H] < -3.5$. Among these objects, three are newly discovered, and one (J0126+0135) is confirmed and analyzed using high-resolution spectra for the first time.

The abundances of C, N, 15 elements from Na to Zn, and 4 neutron-capture elements Sr, Y, Ba, and Eu, have been derived for the sample. When compared with results from the literature, no significant differences have been found. Three out of the eight program stars are regarded as CEMP stars, and one star with enhancement in both carbon and nitrogen has been discovered and classified as a potential CNEMP star.

Efforts have been made to investigate the enrichment of the neutron-capture elements of the EMP stars, especially the distribution of the abundance ratio $[Sr/Ba]$, as well as the comparison between the so-called “mixed” and “unmixed” groups of stars. Our analysis indicates that enlarging the data set of objects with $[Fe/H] < -3.5$ is fairly important to fully understand the nucleosynthesis process of the progenitors of the low-metallicity stars, e.g., the behavior of abundance ratios of neutron-capture elements as well as to further explore the shape and the truth of a cutoff of the low-metallicity tail of the MDF of the Galactic halo. The on-going LAMOST spectro-

scopic survey will be able to improve the situation, and shed light on the nature of Galactic chemical evolution.

We are grateful to the anonymous referee who made valuable suggestions that help improve the paper. H.N.L., G.Z., and W.W. acknowledge support by NSFC grants No. 11103030, 11233004, and 11390371. L.W. is supported by the Young Researcher Grant of National Astronomical Observatories, Chinese Academy of Sciences. N.C. acknowledges support from Sonderforschungsbereich 881 “The Milky Way System” (subproject A4) of the German Research Foundation (DFG). Guoshoujing Telescope (the Large Sky Area Multi-Object Fiber Spectroscopic Telescope, LAMOST) is a National Major Scientific Project built by the Chinese Academy of Sciences. Funding for the project has been provided by the National Development and Reform Commission. LAMOST is operated and managed by the National Astronomical Observatories, Chinese Academy of Sciences. This research uses data obtained through the Telescope Access Program (TAP), which has been funded by the Strategic Priority Research Program “The Emergence of Cosmological Structures” (Grant No. XDB09000000), National Astronomical Observatories, Chinese Academy of Sciences, and the Special Fund for Astronomy from the Ministry of Finance.

REFERENCES

- Aoki, W., Beers, T. C., Christlieb, N., Norris, J. E., Ryan, S. G., & Tsangarides, S. 2007, *ApJ*, 655, 492
- Aoki, W., Suda, T., Boyd, R. N., Kajino, T., & Famiano, M. A. 2013, *ApJ*, 766, L13
- Aoki, W., et al. 2006, *ApJ*, 639, 897
- Asplund, M., Grevesse, N., Sauval, A. J., & Scott, P. 2009, *ARA&A*, 47, 481
- Barklem, P. S., et al. 2005, *A&A*, 439, 129
- Beers, T. C., & Christlieb, N. 2005, *ARA&A*, 43, 531
- Beers, T. C., Preston, G. W., & Shectman, S. A. 1992, *AJ*, 103, 1987
- Beers, T. C., Rossi, S., Norris, J. E., Ryan, S. G., & Shefler, T. 1999, *AJ*, 117, 981
- Bernstein, R., Shectman, S. A., Gunnels, S. M., Mochnacki, S., & Athey, A. E. 2003, in *Society of Photo-Optical Instrumentation Engineers (SPIE) Conference Series*, Vol. 4841, Instrument Design and Performance for Optical/Infrared Ground-based Telescopes, ed. M. Iye & A. F. M. Moorwood, 1694–1704
- Bonifacio, P., et al. 2009, *A&A*, 501, 519
- Bromm, V., & Yoshida, N. 2011, *ARA&A*, 49, 373
- Carollo, D., et al. 2007, *Nature*, 450, 1020
- . 2012, *ApJ*, 744, 195
- Castelli, F., & Kurucz, R. L. 2003, in *IAU Symposium*, Vol. 210, Modelling of Stellar Atmospheres, ed. N. Piskunov, W. W. Weiss, & D. F. Gray, 20P+
- Cayrel, R. 1988, in *IAU Symposium*, Vol. 132, The Impact of Very High S/N Spectroscopy on Stellar Physics, ed. G. Cayrel de Strobel & M. Spite, 345
- Cayrel, R., et al. 2004, *A&A*, 416, 1117
- Chamberlain, J. W., & Aller, L. H. 1951, *ApJ*, 114, 52
- Christlieb, N., Schörck, T., Frebel, A., Beers, T. C., Wisotzki, L., & Reimers, D. 2008, *A&A*, 484, 721
- Christlieb, N., et al. 2002, *Nature*, 419, 904
- Cohen, J. G., Christlieb, N., McWilliam, A., Shectman, S., & Thompson, I. 2011, in *RR Lyrae Stars, Metal-Poor Stars, and the Galaxy*, ed. A. McWilliam, 239
- Cohen, J. G., Christlieb, N., McWilliam, A., Shectman, S., Thompson, I., Melendez, J., Wisotzki, L., & Reimers, D. 2008, *ApJ*, 672, 320
- Cohen, J. G., et al. 2002, *ApJ*, 612, 1107
- . 2005, *ApJ*, 633, L109
- Cui, X.-Q., et al. 2012, *Research in Astronomy and Astrophysics*, 12, 1197
- Demarque, P., Woo, J.-H., Kim, Y.-C., & Yi, S. K. 2004, *ApJS*, 155, 667
- François, P., et al. 2007, *A&A*, 476, 935
- Frebel, A., Casey, A. R., Jacobson, H. R., & Yu, Q. 2013, *ApJ*, 769, 57

- Frebel, A., & Norris, J. E. 2013, *Metal-Poor Stars and the Chemical Enrichment of the Universe*, ed. T. D. Oswalt & G. Gilmore, 55
- Frebel, A., et al. 2005, *Nature*, 434, 871
- , 2006, *ApJ*, 652, 1585
- Gratton, R. G., Carretta, E., Claudi, R., Lucatello, S., & Barbieri, M. 2003, *A&A*, 404, 187
- Gray, R. O., & Corbally, C. J. 1994, *AJ*, 107, 742
- Heger, A., & Woosley, S. E. 2010, *ApJ*, 724, 341
- Höllek, J. K., Frebel, A., Roederer, I. U., Sneden, C., Shetrone, M., Beers, T. C., Kang, S.-j., & Thom, C. 2011, *ApJ*, 742, 54
- Honda, S., Aoki, W., Ishimaru, Y., Wanajo, S., & Ryan, S. G. 2006, *ApJ*, 643, 1180
- Johnson, J. A., Herwig, F., Beers, T. C., & Christlieb, N. 2007, *ApJ*, 658, 1203
- Keller, S. C., et al. 2007, *PASA*, 24, 1
- , 2014, *Nature*, 506, 463
- Lai, D. K., Bolte, M., Johnson, J. A., Lucatello, S., Heger, A., & Woosley, S. E. 2008, *ApJ*, 681, 1524
- Lee, Y. S., et al. 2008, *AJ*, 136, 2022
- Li, H. N., et al. 2010, *A&A*, 521, A10
- Lucatello, S., Beers, T. C., Christlieb, N., Barklem, P. S., Rossi, S., Marsteller, B., Sivarani, T., & Lee, Y. S. 2006, *ApJ*, 652, L37
- Luo, A.-L., et al. 2012, *Research in Astronomy and Astrophysics*, 12, 1243
- McWilliam, A. 1997, *ARA&A*, 35, 503
- McWilliam, A., Preston, G. W., Sneden, C., & Searle, L. 1995, *AJ*, 109, 2757
- Nomoto, K., Kobayashi, C., & Tominaga, N. 2013, *ARA&A*, 51, 457
- Norris, J. E., Ryan, S. G., & Beers, T. C. 1996, *ApJS*, 107, 391
- , 2001, *ApJ*, 561, 1034
- Norris, J. E., et al. 2013a, *ApJ*, 762, 25
- , 2013b, *ApJ*, 762, 28
- Placco, V. M., Frebel, A., Beers, T. C., Christlieb, N., Lee, Y. S., Kennedy, C. R., Rossi, S., & Santucci, R. M. 2014, *ApJ*, 781, 40
- Placco, V. M., Frebel, A., Beers, T. C., Karakas, A. I., Kennedy, C. R., Rossi, S., Christlieb, N., & Stancliffe, R. J. 2013, *ApJ*, 770, 104
- Pols, O. R., Izzard, R. G., Stancliffe, R. J., & Glebbeek, E. 2012, *A&A*, 547, A76
- Qian, Y.-Z., & Wasserburg, G. J. 2007, *Phys. Rep.*, 442, 237
- Rockosi, C., Beers, T. C., Majewski, S., Schiavon, R., & Eisenstein, D. 2009, in *Astronomy*, Vol. 2010, *astro2010: The Astronomy and Astrophysics Decadal Survey*, 14
- Roederer, I. U. 2013, *AJ*, 145, 26
- Ryan, S. G., Norris, J. E., & Beers, T. C. 1996, *ApJ*, 471, 254
- Schörck, T., et al. 2009, *A&A*, 507, 817
- Sneden, C. 1973, *ApJ*, 184, 839
- Sneden, C., et al. 2003, *ApJ*, 591, 936
- Sobeck, J. S., et al. 2011, *AJ*, 141, 175
- Spite, M., Caffau, E., Bonifacio, P., Spite, F., Ludwig, H.-G., Plez, B., & Christlieb, N. 2013, *A&A*, 552, A107
- Spite, M., et al. 2005, *A&A*, 430, 655
- Travaglio, C., Gallino, R., Arnone, E., Cowan, J., Jordan, F., & Sneden, C. 2004, *ApJ*, 601, 864
- Wanajo, S., Kajino, T., Mathews, G. J., & Otsuki, K. 2001, *ApJ*, 554, 578
- Yanny, B., et al. 2009, *AJ*, 137, 4377
- Yong, D., et al. 2013a, *ApJ*, 762, 26
- , 2013b, *ApJ*, 762, 27
- York, D. G., et al. 2000, *AJ*, 120, 1579
- Zhao, G., Chen, Y., Shi, J., Liang, Y., Hou, J., Chen, L., Zhang, H., & Li, A. 2006, *Chinese Journal of Astronomy and Astrophysics*, 6, 265
- Zhao, G., Zhao, Y.-H., Chu, Y.-Q., Jing, Y.-P., & Deng, L.-C. 2012, *Research in Astronomy and Astrophysics*, 12, 723